# Spatially-Segmented Colored Radiative Cooler With Angle-Robustness

Dong Hyun Seo, Se-Yeon Heo, Do Hyeon Kim, Young Min Song, and Gil Ju Lee

***Abstract*—Conventional radiative cooling devices are white or silver in color to achieve high reflectance in the solar spectral range. However, a versatile color that can be applied to the radiative cooler is required for practical application. To determine the boundary between coloration and cooling performance, the reflectance in the visible range should be fine-tuned. Here, this paper presents a spatially-segmented colored radiative cooler (SSCRC), which is a 2-dimensional micro-patterning of colored areas, with angle-robustness. By using the metal-insulator-metal (MIM) optical resonator incorporating high refractive index dielectric (*i.e.,* $TiO_2$), the SSCRC shows consistent coloration in a wide-angle ranging up to 70°. In addition, the spatial segmentation introduced in the colored radiative cooler coordinates the relationship between solar absorption and vivid coloration. We perform the systematic designs in terms of spectrum, thermal analyses, and color coordinates. Finally, experimental demonstrations confirm the theoretical results on the coloration/cooling performance of SSCRC during the daytime.**

***Index Terms*—Angle robustness, colored cooler, metal-insulator-metal, optical resonator, radiative cooling.**

## I. Introduction

In EVERY industry, the demands on eco-friendly technologies have been significantly increased owing to rapid climate change worldwide. The world has struggled to minimize carbon-emission produced from conventional technology, for releasing global warming. In this situation, radiative cooling technologies have been highlighted as one of the next-generation cooling systems. As radiative cooling does not require external energy consumption, the carbon-emission is near zero [1]–[9]. The brilliant advances in radiative cooling have offered various types of coolers such as films [10], paints [11], [12], woods [13], textiles [14], and windows for buildings [15], [16], vehicles [17], [18], solar cells [19]–[21], and even wearable devices [22].

Manuscript received January 14, 2022; revised February 22, 2022; accepted February 26, 2022. Date of publication March 3, 2022; date of current version March 16, 2022. This work was supported in part by the National Research Foundation of Korea under Grants NRF-2021R1C1C2013605, NRF-2020R1A2C2004983, NRF-2018M3D1A1058997, and NRF-2017M3D1A1039288, in part by GIST Research Institute funded by the GIST in 2022, and in part by the Creative Human Resource Education and Research Programs for ICT under Grant BK21FOUR. (*Corresponding authors: Young Min Song; Gil Ju Lee.*)

Dong Hyun Seo, Se-Yeon Heo, Do Hyeon Kim, and Young Min Song are with the School of Electrical Engineering and Computer Science, Gwangju Institute of Science and Technology, Gwangju 61005, Republic of Korea (e-mail: ekdcns22@gm.gist.ac.kr; tpdus0364@gist.ac.kr; ehgus320@gm.gist.ac.kr; ymsong@gist.ac.kr).

Gil Ju Lee is with the Department of Electronics Engineering, Pusan National University, Busan 46241, Republic of Korea (e-mail: gjlee0414@pusan.ac.kr).

Digital Object Identifier 10.1109/JPHOT.2022.3155715

Fundamentally, the cooling potential of radiative coolers proportionally increases to a surface area covered by the cooler [23]. Thus, radiative cooling needs a wide installation space to maximize the cooling performance. For example, in buildings, the cooler is traditionally installed on a rooftop, but the side-wall, which occupies most of the buildings, is also an option to maximize the cooling potential. Recently, directional control of heat emission that can be adjustable for the side-wall cooling has been highlighted [24], [25]. However, the high reflectivity in common radiative coolers seriously hinders using the side-wall because the reflected sunlight can damage adjacent buildings, walking pedestrians, and ecosystems [26]–[28]. For addressing this challenge, colored radiative coolers which consider aesthetic purposes should be developed and optimized. Previously, several groups reported various types of colored radiative coolers such as metal-insulator-metal (MIM) resonator [29], one-dimensional photonic structure [30], multi-grating structure [31], textile [32], and optical film [33], but there is still room for improvement in angle-robustness and solar absorption. In particular, since solar absorption determines the relationship between cooling and coloration, the fine-tunability of solar absorption is required. However, the strategy for this has been barely studied so far.

In this paper, we propose a spatially-segmented colored radiative cooler (SSCRC) with angle-robustness to release the burden of this challenging work. The SSCRC is composed of 2-dimensional micro-patterned metal-insulator-metal (MP-MIM) structures to adjust the areal fraction of colored and uncolored domains. Polydimethylsiloxane (PDMS) encapsulates the structures for broadband emission in the infrared (IR) region [19], [20]. The simple configuration of SSCRC (*i.e.,* MIM and PDMS) accompanies with the facile and affordable fabrication. We investigated the resonance condition in the MIM structure to establish angle-robustness. The optical and thermal analyses also reveal the relationship between coloration and solar absorption. Based on the theoretical results, we fabricated the samples with vivid colors. Moreover, outdoor field tests confirm the cooling features which are estimated from the thermal equilibrium equation [5].

## II. Results and Discussion

### A. Concept of the Spatially-Segmented Colored Radiative Cooler With Angle-Robustness

The proposed SSCRC is depicted in Fig. 1(a). The SSCRC shows a wide-angle tolerant and saturation tunable color with an MP-MIM. The saturation directly controlled by MP-MIM

This work is licensed under a Creative Commons Attribution-NonCommercial-NoDerivatives 4.0 License. For more information, see https://creativecommons.org/licenses/by-nc-nd/4.0/

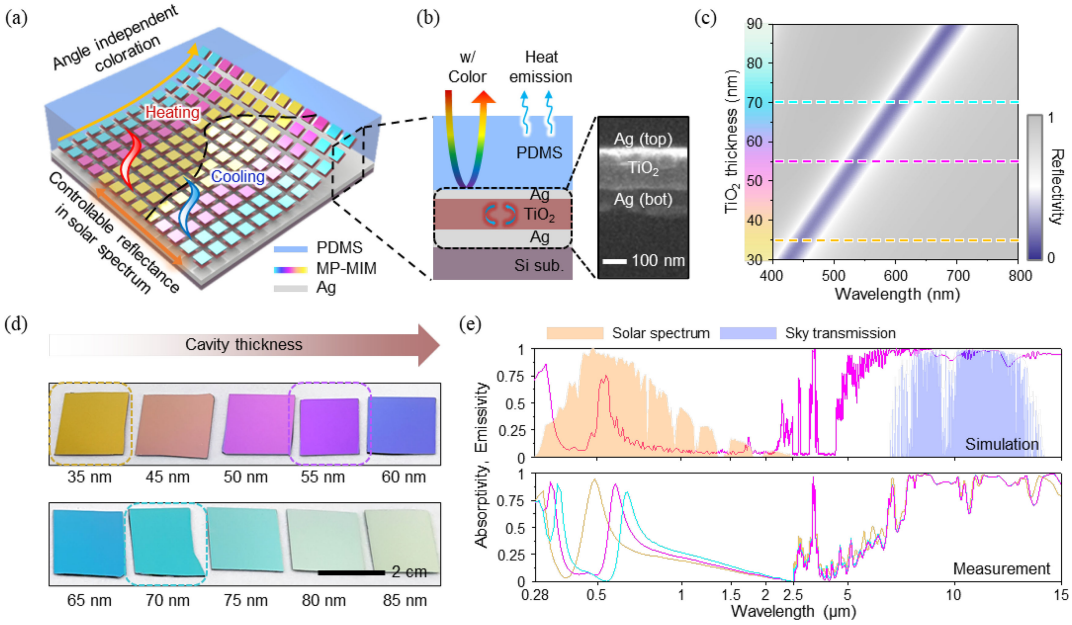


Fig. 1. (a) Schematic of spatially-separated colored radiative cooler (SSCRC) including micro-patterned metal-insulator-metal (MP-MIM) resonator. By controlling the filling fraction of the $TiO_2$ layer, the reflectance within the solar spectrum is tuned. The dashed line separates the cooling area and heating area. (b) Magnified structural view and scanning electron microscope (SEM) image. The PDMS layer (100 $\mu$m) serves as a broadband emitter. The MIM structure consists of top Ag (20 nm)-$TiO_2$(35–85 nm)-bottom Ag (100 nm) layer. The SEM image represents a magenta sample. (c) Calculated reflectivity spectra and color bar of the MIM as a function of $TiO_2$ thickness and wavelength. Each dashed line represents reflectivity spectra of the subtractive color (yellow, magenta, and cyan). (d) Photograph of the fabricated colored radiative cooler as a function of $TiO_2$ cavity thickness. (e) Simulated absorptivity spectra from the visible to the far-infrared wavelength of magenta cooler (upper). Measured absorptivity spectra of yellow, magenta, and cyan cooler through the ultraviolet-visible-near infrared (UV-VIS-NIR) spectrophotometer and Fourier-transform infrared spectrometer (FT-IR).

enables determining the boundary of heating/cooling performance. Fig. 1(b) displays the unit cell in the cross-sectional view of the SSCRC and scanning electron microscope (SEM) image of the fabricated sample. The PDMS of 100 μm emits thermal radiation through the broad IR spectral range due to the high extinction coefficient of PDMS in that region [19]. The Fabry-Perot resonator incorporates a $TiO_2$ cavity inserted between two thin Ag layers (top Ag: 20 nm and bottom Ag: 100 nm). By tunning the thickness and a filling fraction (FF) of the $TiO_2$ cavity, the resonant wavelength and reflectivity of the colored cooler are controlled independently. Thus, it is possible to control hue and saturation finely. The SEM image indicates the fabricated sample of magenta color (*i.e.,* $TiO_2$ of 55 nm).

Fig. 1(c) represents the simulated reflectivity spectra and color bar of the MIM resonator as a function of $TiO_2$ cavity thickness and wavelength. By increasing the cavity thickness, the dip of reflectance is red-shifted (*i.e.,* toward the longer wavelengths) linearly. In Fig. 1(c), the three dashed lines represent the cavity thicknesses corresponding to primary subtractive colors (yellow: 35 nm, magenta: 55 nm, and cyan: 70 nm). To prove the calculated result, the photographs of the fabricated samples are shown in Fig. 1(d). The representative samples of primary subtractive color are marked by dashed lines with each color.

The cooling temperature ($T_{cool}$) for the radiative cooler is calculated by the thermal equilibrium equation (1) [5].

$$P_{rad}\left(T_s\right) - P_{sun} - P_{atm}\left(T_{amb}\right) + h_c\left(T_s - T_{amb}\right) = 0. \tag{1}$$

where $P_{rad}(T_s)$ is the radiation power of the cooler at a temperature of sample ($T_s$), $P_{sun}$ is the incident solar power, $P_{atm}(T_{amb})$ is the absorbed power by incident atmospheric radiation at ambient temperature ($T_{amb}$), and $h_c(T_s - T_{amb})$ is the non-radiative heat exchange term including conductive and convective powers, where $h_c$ is non-radiative heat exchange coefficient. From the (1), the conventional radiative cooler should provide high reflectance within the solar spectrum and thermal emission in IR spectral region including the atmospheric window (*i.e.,* 8–13 μm).

The upper of Fig. 1(e) shows the simulated absorptivity/emissivity spectrum of magenta-colored cooler (*i.e.,* $TiO_2$ of 55 nm). Due to its sharp solar absorption induced by the MIM resonator [29], [34], the cooler shows the designed color with minimal heat gain. Additionally, the encapsulated PDMS radiates heat to outer space through the transparent atmospheric window noted by sky transmission in the graph. The lower of Fig. 1(e) presents measured absorptivity/emissivity spectra of yellow, magenta, and cyan (*i.e.,* $TiO_2$ of 35, 55, and 70 nm, respectively). The fabricated SSCRCs show absorptivity peaks and emissivity spectra which are well-matched with the simulation results.

### B. Angular Tolerant Characteristics in SSCRC

The phase shift during a single round-trip within the Fabry-Perot cavity is given by the sum of two reflections and propagation phase shift [34]–[37]. Thus, the resonance condition is given by (2).

$$\phi_{r21} + \phi_{r23} + \phi_{prop} = 2m\pi. \tag{2}$$

where $\phi_{r21}$ and $\phi_{r23}$ are the phase shift induced by the internal reflection at the interface between metal and insulator, $\phi_{prop}$ is the propagation phase shift originated from the optical path

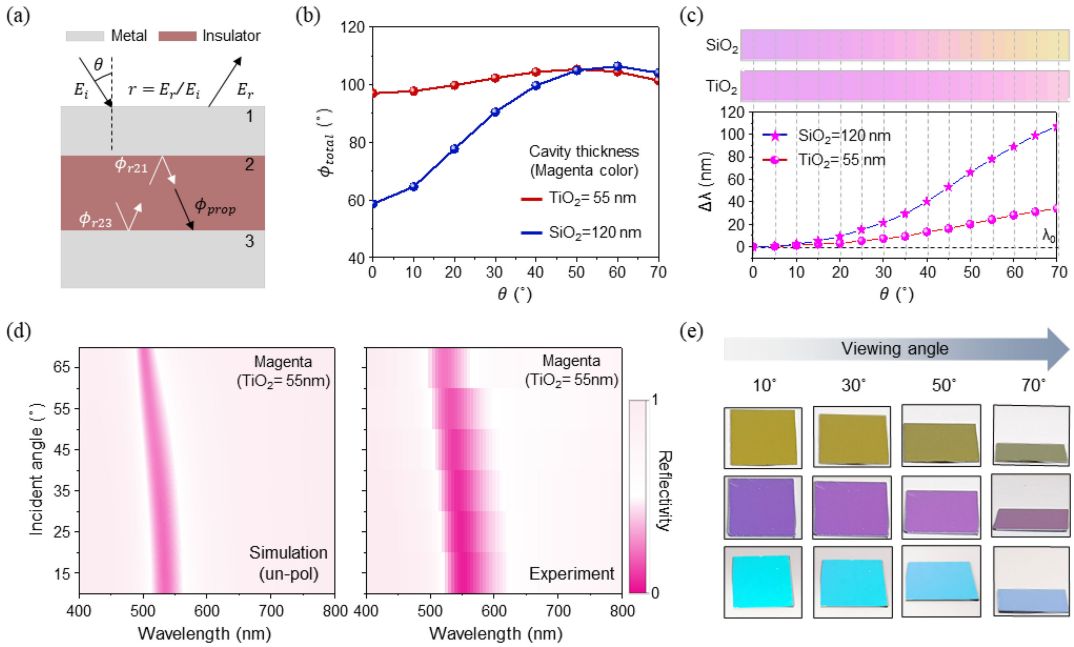


Fig. 2. (a) Schematic of Ag-$TiO_2$-Ag (MIM) resonator and phase shift of incident light. The total reflection coefficient is defined as the amplitude ratio of $E_r$ to $E_i$. (b) Calculated total phase shift ($\phi_{total}$), which is derived from the total reflection coefficient. Due to the negligible total phase shift variation depending on the incident angle in the $TiO_2$ cavity, the resonator exhibits an angle invariant characteristic. (c) Resonant wavelength shift ($\Delta\lambda = \lambda_0$-$\lambda$) as a function of incident angle, $\lambda_0$ is the resonant wavelength at normal incidence. The two-color bar represents hue variation corresponding to each incident angle in MIM containing $SiO_2$ and $TiO_2$ cavity, respectively. (d) Contour maps of calculated reflectivity spectra of unpolarized incident light (left) and measured reflectivity spectra (right) for the magenta resonator. (e) Photographs of the CMY coolers taken from viewing angles 10° to 70°.

difference, and $m$ is a positive integer. Many previous works demonstrated the phase shift is compensated and resonance condition is sustained even at a large incident angle in a high refractive index cavity [34], [35].

Fig. 2(a) exhibits the schematic of the MIM resonator. The light enters with the angle of incidence ($\theta$) and undergoes phase shift including the two reflections and propagation phase shift. The amplitude of incident and reflected light are denoted by $E_i$ and $E_r$, respectively. We calculate the total phase shift ($\phi_{total}$) from the total reflection coefficient $r$ (3), which is defined as the ratio of the reflected amplitude to incident amplitude, to investigate angle-robustness in the MIM.

$$\phi_{total} = \tan^{-1}\left(\mathrm{Im}\{r\}/\mathrm{Re}\{r\}\right) . \tag{3}$$

where $\phi_{total}$ is the total phase shift, $r$ is a complex total reflection coefficient, $\mathrm{Im}\{r\}$ is imaginary part of the total reflection coefficient, and $\mathrm{Re}\{r\}$ is real part of the total reflection coefficient. Fig. 2(b) shows the two total phase shifts that occur in the high refractive index (*i.e.,* $TiO_2$) and low refractive index (*i.e.,* $SiO_2$). The two cavities emanate the same magenta color; however, each cavity thickness is different due to the difference in refractive index. In the $TiO_2$ cavity, the initial phase is kept at the overall incident angle (*i.e.,* the maximum phase shift is 8° at the incident angle of 50°) whereas the $SiO_2$ cavity shows abrupt phase change in the range of 10–50°. The maximum phase shift is 48° at the incident angle of 60°.

The resonant wavelength shifts to satisfy the resonance condition which is modified by different angles of incidence. Fig. 2(c) exhibits the difference of resonant wavelength between a normal incidence and an oblique incidence ($\Delta\lambda = \lambda_0 - \lambda$, where the $\lambda_0$ is the resonant wavelength at a normal incident angle). Same with the result in Fig. 2(b), the $TiO_2$ cavity shows an angle-independent characteristic with a small resonant wavelength shift. The wavelength decreases by 34 nm until the incident angle of 70° in the $TiO_2$ cavity (Fig. 2(c); bottom). However, the $SiO_2$ cavity shows a large resonant wavelength shift (*i.e.,* the difference of resonant wavelength is 107 nm at the incident angle of 70°) Additionally, the calculated color representation corresponding to each cavity and incident angle is illustrated in Fig. 2(c) (upper). The resonant wavelength is blue-shifted (*i.e.,* toward the shorter wavelengths) as the incident angle increase from 10° to 70°. Thus, the hue is changed from magenta to yellow.

For accurate comparison with the fabricated cooling device, a numerical calculation of the reflectivity spectra of magenta at various angles was performed under the unpolarized light (Fig. 2(d); left). Then, the angular insensitive characteristic was measured and confirmed using a variable-angle specular reflectance accessory (VARSA) for the angle of 15–65° (Fig. 2(d); right). The measured reflectivity spectra depending on the viewing angle are well-matched with the calculated result. The photographs of the fabricated samples with subtractive primary colors (cyan, magenta, and yellow; CMY) illuminated by different oblique angles of incidence are shown in Fig. 2(e). The initial colors are sustained even at a large viewing angle (70°).

### *C. Half-Tone Coloration for Radiative Cooling Based on Spatially-Segmented Colored Areas*

The total solar intensity during the daytime is near 1000 W/m$^2$ [19]. Due to the strong solar irradiation, despite the minimal loss of visible reflectance, the color disturbs that the temperature of

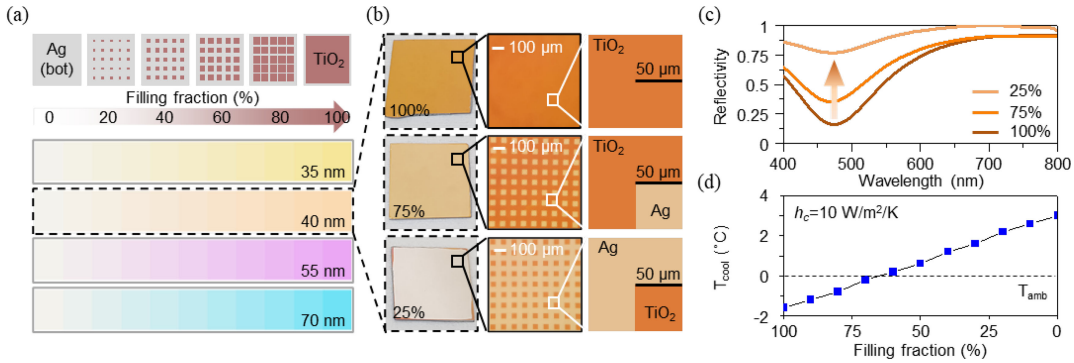


Fig. 3. (a) Color representations of SSCRC as a function of filling fraction (FF). The half-tone color of orange (*i.e.*, $TiO_2$ of 40 nm) is chosen to investigate the reflectivity variation and cooling temperature with FF variation. The PDMS encapsulation is not presented here. (b) Photographs (left), microscope images (middle), and magnified schematics (right) of the SSCRC with different FF. In the low FF of the $TiO_2$ cavity, the saturation of the sample is also decreased. (c) Measured reflectivity spectra of the SSCRC. By controlling the FF, reflectivity is tuned. (d) Calculated cooling temperature ($T_{cool} = T_{amb}$-$T_s$) of the selected half-tone colored cooler with a variation of FF. The dashed black line indicates the temperature of ambient ($T_{amb}$). To accurately compare with practical situations, the non-radiative heat exchange coefficient ($h_c$) is set to 10 W/m$^2$/K. From the result in Fig. 3(c) and (d), by tunning the reflectivity within visible spectral range, the sub-ambient cooling performance can be achieved during the daytime.

the device drops below ambient temperature. Therefore, most colored radiative coolers are limited as near-ambient cooling. Consequently, to achieve both coloration and sub-ambient cooling temperature, it is needed that control for solar reflectance more in the visible range. The solar reflection of the SSCRC is directly controlled by the filling fraction of the $TiO_2$ dielectric layer.

Fig. 3(a) illustrates color representations of SSCRC as a function of filling fraction of $TiO_2$ layer. The hue of the SSCRC is preserved, however, the saturation is tuned with the filling fraction. The half-tone sample (*i.e.,* $TiO_2$ of 40 nm) is chosen to discriminate with other CMY-colored samples. Fig. 3(b) displays the photographs, microscope images, and magnified schematics of fabricated half-tone colored coolers with FF of 100% (Fig. 3(b); upper), 75% (Fig. 3(b); middle), 25% (Fig. 3(b); lower), respectively. The area covered with the $TiO_2$ insulator layer in FF of 25% is replaced by the Ag metal layer in FF of 75%. Thus, we fabricated the two samples with different FF by using the same shadow mask. As the FF of MIM area in SSCRC decreases from 100% to 25%, the reflectivity in the visible spectral range increase without the resonant wavelength shift (Fig. 3(c)). The simulated cooling temperature ( $T_{cool} = T_{amb} - T_s$) as a function of the filling fraction is shown in Fig. 3(d). In lower than FF of 60%, the cooling temperature is over zero (*i.e.,* the temperature of cooler below the ambient temperature). To contemplate practical conditions, the cooling temperatures are calculated with $h_c$ of 10 W/m$^2$/K. The simulated result implies that the cooler can be applied to sub-ambient cooling during the daytime.

### *D. Cooling Performance of SSCRCs With Primary Colors and Halt-Tone Colors*

The outdoor measurement setup was placed on a rooftop at Gwangju Institute of Science and Technology (GIST), South Korea, to investigate the cooling performance of SSCRCs (Fig. 4(a) and (b)). The wooden frame is covered with Aluminum (Al) foil, which served as a parasitic heat shield by reflecting the sunlight. The samples are placed on a polystyrene block, which was wrapped by Al foil and supported by a clear acrylic box. The detailed information about the setup is given in the previously published research paper [5], [29]. In Fig. 4(b), the left-side samples (cyan, magenta, yellow, and black) represent the hue variation group and the right-side samples (half-tone with FF of 100%, 75%, 50%, and 0%) represent saturation variation group.

As expected, the black emitter, which absorbs most of the visible light, shows the highest temperature compared to the CMY sample. Among the CMY-colored coolers, the yellow (*i.e.,* $TiO_2$ of 35 nm) shows a higher temperature compared to other samples (magenta, cyan) (Fig 4(c); middle). It originates from the high and wide absorptivity in the visible spectral range as shown in Fig. 1(e). However, despite the vivid color covering the whole area of the cooler, the average temperature differences ($\Delta T = T_s - T_{amb}$) are 1.4 °C (cyan), 1.9 °C (magenta), and 2.2 °C (yellow) during the daytime. Therefore, they maintains the near-ambient temperature, but still heating status.

Fig. 4(d) indicates the measured data of half-tone-colored coolers. As decreases the FF value, the cooling performance is increased. The temperature of the full FF (*i.e.,* $TiO_2$ of 40 nm; FF of 100%) cooler is similar to the CMY-colored cooler, however, the temperature of the lower FF sample is below that of the 100% FF sample (Fig. 4(d); middle). Notably, the FF of the 25% sample shows the temperature below ambient temperature. The average temperature differences ($\Delta T$) are 1.5 °C (FF of 100%), 0.5 °C (FF of 75%), and -1.2 °C (FF of 25%) during the daytime (Fig. 4(d); lower). The experiment is maintained for over 6 hours during which period the average solar power exceeded 683 W/m$^2$ (Fig. 4(c) and (d); upper). The measurement result demonstrates the SSCRC can be applied to sub-ambient cooling by controlling the reflectance within the solar spectrum.

## III. Materials and Methods

### *A. Fabrication of the SSCRC*

The bottom Ag of 100 nm was deposited using electron beam evaporation (KVE-E2000, Korea Vacuum Tech Ltd, Korea) on sing-side polished silicon (100) wafer. After forming the bottom Ag layer, the hexamethyldisilane (HMDS) was spin-coated at

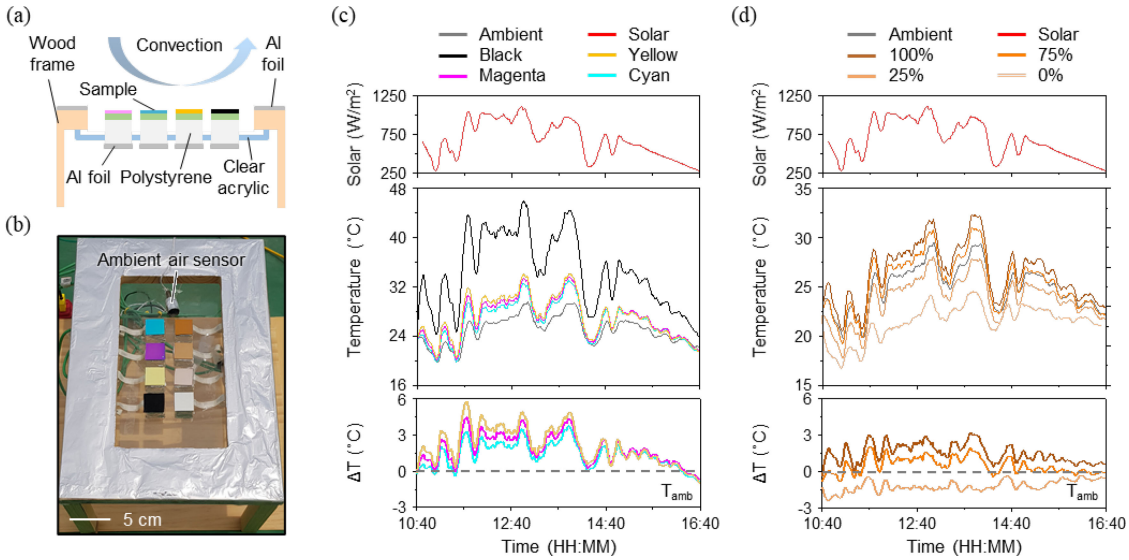


Fig. 4. (a) Schematic and (b) photograph of the measurement setup on the rooftop. (c) Temperature measurements obtained from the measurement setup with hue variation (CMY) group and (d) saturation variation (FF variation) group during the six hours. The top of Fig. 4(c) and (d) represent the solar irradiation during the measurement. The middle of Fig. (c) and (d) indicate the temperature of various colored coolers, and black emitter, compared with the ambient air temperature during the daytime. The bottom of Fig. 4(c) and (d) show the difference between the sample temperature and ambient air temperature ($\Delta T = T_s$-$T_{amb}$) of each group (hue and saturation), respectively.

5000 rpm for 30 sec and annealed on a hot plate at 110 °C for 1 min to increase the adhesion of positive photoresist (PR; AZ5214 E, MicroChemicals, Germany). The PR was deposited by spin coating at 5000 rpm for 30 sec and soft baked on a hot plate at 110 °C for 70 sec. Next, the sample was exposed under 365-nm ultraviolet (UV) light for 12 sec with a pre-patterned mask according to FF. After the photolithography, the PR was developed by immersion in a developer (AZ-MIF-300, MicroChemicals, Germany) for 1 min. The post-baking process was performed to harden the patterned PR on a hot plate at 110 °C for 2 min. Last, the residual PR was removed by acetone. For the $TiO_2$ cavity formation, different rate of electron beam deposition was adapted according to the sample color (*i.e.,* 0.2 Å/s $\sim$ 0.8 Å/s). After forming the $TiO_2$ cavity, a 20-nm-thick Ag was deposited by electron beam evaporation. Next, The PDMS which was mixed with an agent: base ratio of 1:10 is degassed before spin coating on the MIM structure. The spin coating condition is 800 rpm for 30 sec to form 100-$\mu$m-thick PDMS. Finally, the fabricated sample was annealed on a hot plate at 110 °C for 2 min.

### *B. Optimization and Numerical Simulation*

The optical characteristics including reflectance, absorbance, and transmittance are simulated using commercial software (Diffract MOD, RSoft Design Group, Synopsys, USA) based on the rigorous coupled-wave analysis (RCWA). The cavity thickness and FF are also optimized by the RCWA simulation method. The silvery and colored areas in SSCRC are considered in the simulations to reflect the effect of patterning. To calculate the optical efficiency of the proposed photonic structure, a square grid size of 0.1 nm was used in the RCWA simulation. Complex refractive index and material dispersion were also considered to obtain a reasonable output. The complex refractive indices of $TiO_2$ and PDMS were obtained from previous research [38], [39]. The Drude model was used for considering material dispersion of the Ag layer.

The cooling temperature was estimated from the obtained emissivity spectra through the RCWA and thermal equilibrium equation calculated by MATLAB (MathWorks Inc., USA).

## IV. Conclusion

In this paper, we introduced a spatially-segmented colored radiative cooler for angle-robust coloration and sub-ambient cooling performance. In order to reduce the color variation by viewing angle, our structure consists of the high refractive index cavity ($TiO_2$) in the optical resonator, which can minimize the variation of total reflection phase shift. The proposed SSCRCs emanate diverse color changes in terms of hue and saturation values by the variation of cavity thickness and FF, respectively. In addition, the PDMS, which emits the heat through the broad IR spectral region, is coated on the sample and enables the temperature of the samples to keep near-ambient air temperature.

The simulated results demonstrate that resonant wavelength in MIM including the $TiO_2$ cavity is kept under a wide incident angle (70°). Thus, the high index cavity more preserves its normal incident color than the low index cavity (*i.e.*, $SiO_2$) at a large viewing angle. The fabricated samples exhibited the subtractive primary colors (CMY), optimized by the numerical simulation method, regardless of viewing angle.

For fine tunability between cooling and coloration, we introduced spatially-segmented MIM resonator to control the reflectivity. We also confirmed the direct relationship between reflectivity and FF for the cavity through the measurement and color variation. The numerical calculation of cooling temperature shows that the SSCRC can achieve sub-ambient cooling by controlling the FF.

Outdoor measurement proved the cooing performance of the fabricated SSCRCs in a real situation. The subtractive primary-colored coolers showed near-ambient cooling. The heating temperature compared with ambient air was under 6 °C in the yellow sample during the daytime. However, the half-tone-colored samples demonstrated sub-ambient cooling during the daytime. The maximum cooling temperature was 2.4 °C at the half-tone colored sample with an FF of 25%. Consequently, our research provides a new way to control the coloration/cooling performance for radiative cooling.

## REFERENCES


[1] H. –Y. Chan, S. B. Riffat, and J. Zhu, "Review of passive solar heating and cooling technologies," *Renewable Sustain. Energy Rev.*, vol. 14, no. 2, pp. 781–789, Feb. 2010.

[2] G. Smith and A. Gentle, "Radiative cooling: Energy savings from the sky," *Nature Energy*, vol. 2, no. 9, pp. 1–2, Sep. 2017.

[3] A. P. Raman, M. A. Anoma, L. Zhu, E. Rephaeli, and S. Fan, "Passive radiative cooling below ambient air temperature under direct sunlight," *Nature*, vol. 515, no. 7528, pp. 540–544, 2014.

[4] X. Sun, Y. Sun, Z. Zhou, M. A. Alam, and P. Bermel, "Radiative sky cooling: Fundamental physics, materials, structures, and applications," *Nanophotonics*, vol. 6, no. 5, pp. 997–1015, 2017.

[5] J. -L. Kou, Z. Jurado, Z. Chen, S. Fan, and A. J. Minnich, "Daytime radiative cooling using near-black infrared emitters," *ACS Photon.*, vol. 4, no. 3, pp. 626–630, 2017.

[6] J. Mandal *et al.*, "Hierarchically porous polymer coatings for highly efficient passive daytime radiative cooling," *Science*, vol. 362, no. 6412, pp. 315–319, 2018.

[7] J. Song, J. Seo, J. Han, J. Lee, and B. J. Lee, "Ultrahigh emissivity of grating-patterned PDMS film from 8 to 13 μm wavelength regime," *Appl. Phys. Lett.*, vol. 117, no. 9, 2020, Art. no. 094101.

[8] Z. Chen, L. Zhu, A. Raman, and S. Fan, "Radiative cooling to deep sub-freezing temperatures through a 24-h day–night cycle," *Nature Commun.*, vol. 7, no. 1, pp. 1–5, 2016.

[9] G. J. Lee, S. Y. Heo, S. Son, K. M. Kang, H. Lee, and Y. M. Song, "Ultra-thin and near-unity selective emitter for efficient cooling," *Opt. Exp.*, vol. 29, no. 20, pp. 31364–31375, 2021.

[10] S. Meng *et al.*, "Scalable dual-layer film with broadband infrared emission for sub-ambient daytime radiative cooling," *Sol. Energy Mater. Sol. Cells*, vol. 208, May. 2020, Art. no. 110393.

[11] D. Chae, S. Son, H. Lim, P. -H. Jung, J. Ha, and H. Lee, "Scalable and paint-format microparticle-polymer composite enabling high-performance daytime radiative cooling," *Mater. Today Phys.*, vol. 18, May. 2021, Art. no. 100389.

[12] S. Atiganyanun *et al.*, "Effective radiative cooling by paint-format microsphere-based photonic random media," *ACS Photon.*, vol. 5, no. 4, pp. 1181–1187, 2018.

[13] T. Li *et al.*, "A radiative cooling structural material," *Science*, vol. 364, no. 6442, pp. 760–763, May 2019.

[14] S. Zeng *et al.*, "Hierarchical-morphology metafabric for scalable passive daytime radiative cooling," *Science*, vol. 373, no. 6555, pp. 692–696, Aug. 2021.

[15] M. Kim, D. Lee, S. Son, Y. Yang, H. Lee, and J. Rho, "Visibly transparent radiative cooler under direct sunlight," *Adv. Opt. Mater.*, vol. 9, no. 13, Jul. 2021, Art. no. 2002226.

[16] Z. Yi *et al.*, "Energy saving analysis of a transparent radiative cooling film for buildings with roof glazing," *Energy Built Environ.*, vol. 2, no. 2, pp. 214–222, Apr. 2021.

[17] S.-Y. Heo *et al.*, "A Janus emitter for passive heat release from enclosures," *Sci. Adv.*, vol. 6, no. 36, eabb 1906, Sep. 2020.

[18] D. H. Kim, G. J. Lee, S. -Y. Heo, il.-S. Kang, and Y. M. Song, "Thermostat property of janus emitter in enclosures," *Sol. Energy Mater. Sol. Cells*, vol. 230, no. 1, May 2020, Art. no. 111173.

[19] S.-Y. Heo, D. H. Kim, Y. M. Song, and G. J. Lee, "Determining the effectiveness of radiative cooler-integrated solar cells," *Adv. Energy Mater.*, 2021, Art. no. 2103258. [Online]. Available: https://doi.org/10.1002/aenm.202103258

[20] L. Zhu, A. Raman, K. X. Wang, M. A. Anoma, and S. Fan, "Radiative cooling of solar cells," *Optica*, vol. 1, no. 1, pp. 32–38, Jul. 2014.

[21] B. Zhao, M. Hu, X. Ao, and G. Pei, "Performance analysis of enhanced radiative cooling of solar cells based on a commercial silicon photovoltaic module," *Sol. Energy*, vol. 176, pp. 248–255, Dec. 2018.

[22] M. H. Kang *et al.*, "Outdoor-useable, wireless/battery-free patch-type tissue oximeter with radiative cooling," *Adv. Sci.*, vol. 8, 2021, Art. no. 2004885.

[23] D. Zhao *et al.*, "Subambient cooling of water: Toward real-world applications of daytime radiative cooling," *Joule*, vol. 3, no. 1, pp. 111–123, 2019.

[24] L. Zhou *et al.*, "Hybrid concentrated radiative cooling and solar heating in a single system," *Cell Reports Phys. Sci.*, vol. 2, no. 2, 2021, Art. no. 100338.

[25] J. Xu, J. Mandal, and A. P. Raman, "Broadband directional control of thermal emission," *Science*, vol. 372, no. 6540, pp. 393–397, 2021.

[26] M. Schiler and E. Valmont, "Urban environmental glare: The secondary consequence of highly reflective materials," in *Proc. 23rd Conf. Passive Low Energy Architecture*, Geneva, Switzerland, Sep. 2006, pp. 6–8.

[27] J. Y. Suk, M. Schiler, and K. Kensek, "Reflectivity and specularity of building envelopes: How materiality in architecture affects human visual comfort," *Architectural Sci. Rev.*, vol. 60, no. 4, pp. 256–265, 2017.

[28] N. J. Shih and Y. S. Huang, "A study of reflection glare in Taipei," *Building Res. Inf.*, vol. 20, no. 1, pp. 30–39, 2001.

[29] G. J. Lee, Y. J. Kim, H. M. Kim, Y. J. Yoo, and Y. M. Song, "Colored, daytime radiative coolers with thin-film resonators for aesthetic purposes," *Adv. Opt. Mater.*, vol. 6, no. 22, 2018, Art. no. 1800707.

[30] W. Li, Y. Shi, Z. Chen, and S. Fan, "Photonic thermal management of coloured objects," *Nat. Commun.*, vol. 9, no. 1, 2018, Art. no. 4240.

[31] L. Zhu, A. Raman, and S. Fan, "Color-preserving daytime radiative cooling," *Appl. Phys. Lett.*, vol. 103, no. 22, 2013, Art. no. 223902.

[32] L. Cai *et al.*, "Temperature regulation in colored infrared-transparent polyethylene textiles," *Joule*, vol. 3, no. 6, pp. 1478–1486, 2019.

[33] J. W. Cho, E. J. Lee, and S. K. Kim, "Full-color solar-heat-resistant films based on nanometer optical coatings," *Nano Lett.*, vol. 22, no. 1, pp. 380–388, 2022.

[34] K. T. Lee, S. Seo, and L. J. Guo, "High-color-purity subtractive color filters with a wide viewing angle based on plasmonic perfect absorbers," *Adv. Opt. Mater.*, vol. 3, no. 3, pp. 347–352, 2015.

[35] C. S. Park, V. R. Shrestha, S. S. Lee, E. S. Kim, and D. Y. Choi, "Omni-directional color filters capitalizing on a nano-resonator of Ag-$TiO_2$-Ag integrated with a phase compensating dielectric overlay," *Sci. Reports*, vol. 5, no. 1, pp. 1–8, 2015.

[36] M. A. Kats, R. Blanchard, P. Genevet, and F. Capasso, "Nanometre optical coatings based on strong interference effects in highly absorbing media," *Nature Mater.*, vol. 12, no. 1, pp. 20–24, 2013.

[37] N. Anous, T. Ramadan, M. Abdallah, K. Qaraqe, and D. Khalil, "Planar asymmetric nano-resonators for highly angle tolerant trans-reflective color filters," *OSA Continuum*, vol. 2, no. 3, pp. 890–904, 2019.

[38] R. Kitamura, L. Pilon, and M. Jonasz, "Optical constants of silica glass from extreme ultraviolet to far infrared at near room temperature," *Appl. Opt.*, vol. 46, no. 33, pp. 8118–8133, 2007.

[39] J. Kischkat *et al.*, "Mid-infrared optical properties of thin films of aluminum oxide, titanium dioxide, silicon dioxide, aluminum nitride, and silicon nitride," *Appl. Opt.*, vol. 51, no. 28, pp. 6789–6798, 2012.